



Multi-objective energy management of multiple microgrids under random electric vehicle charging

Bifei Tan, Haoyong Chen *

School of Electric Power Engineering, South China University of Technology, Guangzhou, 510641, Guangdong Province, China



ARTICLE INFO

Article history:

Received 22 October 2019

Received in revised form

3 May 2020

Accepted 9 July 2020

Available online 25 July 2020

Keywords:

Multi-microgrids

Electric vehicles

Long short-term memory

Consistency algorithm

Pareto optimality

Shannon-Wiener index

ABSTRACT

In view of the increasing development of decentralized power systems and electric vehicles, this paper seeks to improve the energy management performance of multiple microgrid systems under the uncertainty associated with electric vehicle charging. A multi-objective optimization model is established for minimizing the transmission losses, operating costs, and carbon emissions of multiple microgrid systems. Firstly, a novel method is proposed for forecasting electric vehicle charging loads based on a back propagation neural network improved by long short-term memory deep learning. Based on the forecast data, a double layer solution algorithm is proposed, which consists of an adaptive multi-objective evolutionary algorithm based on decomposition and differential evolution at the multiple microgrids layer and a modified consistency algorithm for fast economic scheduling at the single microgrid layer. Finally, a model system composed of four interconnected IEEE microgrids is simulated as a case study, and the performance of the proposed algorithm is compared with that of conventional multi-objective evolutionary algorithms based on decomposition. The simulation results demonstrate the superiority of the global search performance and the rapid convergence performance of the proposed improved algorithm.

© 2020 Elsevier Ltd. All rights reserved.

1. Introduction

Currently, microgrid system technology has become increasingly implemented due to its environmental benefits. It also has a pronounced potential for the flexible integration of numerous power sources, such as large-scale power grids, photovoltaic (PV) units, wind turbines (WTs), diesel engines (MTs), and fuel cells (FCs) [1,2]. Generally, the flexibility of this technology enables local operators to achieve different goals by adjusting the scheduling [3]. To reflect the tradeoff between the economic and environmental benefits, the economic emission dispatch (EED) problem of microgrids has also received the attention of researchers [4].

Current research focuses on the multi-objective optimization of microgrids according to two aspects. Some researchers simplified the multi-objective problem by transforming the objective functions. In the microgrid model proposed by Pourghasem et al., the exchange market algorithm and weighted sum method are employed to combine three conflicting objectives, which are then

transformed as a single objective problem [5]. Similarly, Goudarzi et al. introduced price penalty factors to convert four objective functions to a single objective function [6]. In the proposed islanded microgrid model, Dey used the least and best price penalty factors to convert two single objective problems into a multi-objective problem [7].

In contrast, some researchers have sought to obtain a Pareto set by non-dominated algorithms without converting the objective functions. Ma et al. used change detection and memory-based selection strategies to obtain non-dominated sorting solutions [8]. Chandrasekaran et al. implemented a cuckoo search algorithm and fuzzy set theory in a multi-objective microgrid dispatch model to obtain a best compromise solution from the Pareto-optimal set [9]. Li et al. employed interval optimization to build a model for the multi-objective optimal dispatch of microgrids, and then solved the model using a chaotic group search optimizer with multiple producers [10]. After building different energy storage scenarios in multi-objective modeling, Coelho et al. searched candidate non-dominated solutions from the pool of feasible solutions obtained during different Branch and Bound optimizations [11]. These current research efforts have demonstrated that multi-objective models are often effective in accounting for conflicts and

* Corresponding author. South China University of Technology, Guangzhou, China.

E-mail address: ehychen@scut.edu.cn (H. Chen).

Nomenclature

Abbreviations

DS	distribution system
DG	distributed generation
MG	microgrid
EV	electric vehicle
LSTM	long short-term memory
BPNN	back propagation neural network
MMG	multiple microgrid
SMG	single microgrid
MOEA/D	multi-objective evolutionary algorithm based on decomposition
CA	consistency algorithm
MPC	maximum point of curvature
MP	middle point
ZPSD	zero point of second derivative
NC	no change
DE	differential evolution
PV	photovoltaic
WT	wind turbine
MT	diesel engine
FC	fuel cell
SWI	Shannon-Wiener index
PF	power flow
$\tanh(x)$	tanh function

Parameters: BPNN

w_{ij}^l	connection weight between the j -th neuron in the $(l-1)$ -th layer and the i -th neuron in the l -th layer
b_i^l	offset of the i -th neuron in the l -th layer
$E(i)$	training error for a single sample
N_h	number of neurons in the hidden layer
N_{in}	number of neurons in the input layer
N_{out}	number of neurons in the output layer
a	learning rate
$og/ig/fg$	output/input/forget gate matrix
$L_{g,j}^{train}$	charging load of EVs
$w_g/w_{ih}/w_{ix}$	network weights
$d_k(i)$	i -th training sample in the training sample set
N_{BP}	training sample set
α	learning rate
$LSTM$	
ER_{tol}^{it}	overall error
ER_j	error at period j
$L/H/G/C$	intermediate variables of training set
D	inspection data

igi	output vector of the input gate
$w_{ix}/w_{igc}/w_{ih}$	network weights of the input gate
fgi	output vector of the forget gate
$w_{fx}/w_{fgc}/w_{fh}$	network weights of the forget gate
ogi	output vector of the output gate
$w_{ox}/w_{ogc}/w_{oh}$	network weights of the output gate
θ	adaptive optimization operator
MMG	
C_{MPC}	approximate curves
C_{MP}	approximate curves
C_{ZPSD}	approximate curves
V_{\min}/V_{\max}	lower/upper bound of voltage magnitude
N_{MGs}	number of microgrids
N_{MT}^j	number of diesel generators in microgrid j
$a_{j,k} b_{j,k} c_{j,k}$	parameters determined by gas turbine unit k in the j -th microgrid
$P_{WT,j}$	active power output of the j -th WT unit
$k_{WT,j}$	cost coefficient of the j -th WT unit
$P_{PV,j}$	active power output of the j -th PV unit
$k_{PV,j}$	cost coefficient of the j -th PV unit
N_{PV}	number of PV units
L_{HVNG}	calorific value of natural gas
C	total operating cost of a multi-microgrid system
C_{MT}	fuel cost and operation cost of MTs
C_{FC}	natural gas fuel cost and operation cost of FCs
C_{PV}	operation cost of PV arrays
C_{WT}	operation cost of WTs
u_i^t/u_j^t	voltage at node i/j in the t -th period
$re(\cdot)$	real part
δ_{ij}^t	phase angle difference between nodes i, j .
$g_{MT,i}$	carbon emission coefficient of the i -th gas turbine
$g_{FC,i}$	carbon emission factors of the i -th FC unit
$P_{MT,\min,i}/P_{MT,\max,i}$	minimum/maximum output of MT unit i
$P_{FC,\min,i}/P_{FC,\max,i}$	minimum/maximum output of FC unit i
$P_{MT,d,\max,i}/P_{MT,u,\max,i}$	maximum slope/uphill rate of MT unit i
$P_{FC,d,\max,i}/P_{FC,u,\max,i}$	maximum slope/uphill rate of FC unit i
$P_{pv,I}$	planned output of the i -th PV array at period t
$P_{pv,i}^t$	maximum predicted output for PV i at period t
$P_{trans,max}$	upper transmitted electric power limit between microgrids
$r_{j,k}^{n+1}$	incremental discharge of unit k at iteration $n+1$
$P_{MT,j,k}^{n+1}$	output power of unit k at iteration $n+1$
$P_{L,j,k}^{n+1}$	predicted difference between output power of unit i and load demand
ϵ	positive feedback coefficient
$N_{nb,i}^+$	input type neighborhood set of the i -th unit

tradeoffs between different objectives. However, empirically-based penalty factors are usually adopted to represent their weights, which cannot obtain a convincing Pareto front. Moreover, with the integration of multiple neighboring microgrids and large-scale power grids, the number of variables and parameters will increase significantly, leading the unacceptably increasing error caused by empirically-based parameters [12].

Meanwhile, the penetration of electric vehicles (EVs) in recent years has had a pronounced effect on the reliability of local microgrids owing to the uncertainty of accessed charging loads

[13]. These random charging loads not only can alter the local load characteristics, but also affect the voltage and frequency of power grids, which eventually affects the scheduling capabilities of local microgrids [14]. Therefore, similar to the dispatch method, the development of a method for managing EV charging loads is required to improve the energy management performance of multiple microgrid systems, which has a more complicated topology and more frequent energy transfer [15,16].

Progress has been made over the past few years in the optimal dispatch of microgrids containing EVs, and this work can be divided

into two aspects. Some researchers considered EVs as controllable units that can be employed as independent variables in the dispatch model [17,18]. Lu et al. treated the batteries of the accessed EVs as a kind of mobile distributed energy storage device in the model during the multi-objective optimal dispatch of microgrids [19]. To avoid the energy constraint, Han et al. enforced EV discharge based on the statistical analysis of a regulation signal [20]. In the energy management model of microgrids proposed by Esmaili et al., range anxiety was introduced to encourage users to participate in V2G service, where EVs were considered as distributed energy storage systems [21]. Iacobucci et al. simulated aggregate storage availability from shared autonomous EVs (SAEVs) based on transport patterns, and thereby optimized EV charging. The economic potential for SAEVs to act as storage in a microgrid was furthermore described in another work [22].

Because the number of EVs is gradually increasing, some researchers believed that considering a large number of EVs as independent variables may lead to convergence deterioration [23]. This has led to attributing greater engineering significance to regarding EVs in each microgrid as a group, and predicting EV charging load trends through historical data [24,25]. Based on charging data from an energy control center, Hao et al. used a clustering algorithm and artificial neural network (ANN) to build a power forecasting model that could effectively characterize the uncertainty of EV charging loads [26]. As an improvement of their work in 2017 [19], Lu et al. addressed the uncertainties of stochastic EV access using Monte Carlo simulation and analyzed the influence of a cost weighting factor on multi-objective scheduling results [27]. However, the studies mentioned above have usually focused on the modeling of batteries based on a conventional mathematical model, which may be affected by the intrinsic properties of the model. The research of Jahangir et al. demonstrated that a data-driven ANN can provide a new solution for EV charging load prediction [28]. Moreover, based on historical data, an ANN can construct the mapping relationship between certain variables, such as wind speed and humidity [29] and the probabilistic power-flow input and its output [30,31]. In this way, ANN-based methods exhibit a good ability to forecast the behavior of different highly uncertain phenomena.

This paper presents a novel energy management framework, as illustrated in Fig. 1, that facilitates the forecast of EVs charging loads and multi-objective optimization scheduling. It's formulated as a two-stage EED where the forecast problem aims at minimizing forecast errors of EVs charging loads and the multi-objective problem optimizes the total MMG costs while minimizing network line loss and carbon emission. A novel multi-objective approach is proposed in this paper to find the non-dominated solution set of the system operation. The main contributions of this paper are identified as follows.

1. In the forecast part, the proposed model first considers the time of day and temperature as the relevant variables dictating the charging loads of EVs, uses the BPNN for model training, and then applies a modified form of the LSTM deep learning approach to correct the trained network.
2. After a multi-model approximation for MT characteristics, a modified consistency algorithm (CA) is adopted for fast economic scheduling at the single microgrid layer.
3. Considering the constraints of renewable sources and energy transmission, an adaptive Tchebycheff-based MOEA/D and differential evolution (DE) is adopted at the multiple microgrids layer based on the resulting EVs charging load data.

4. The comparison of the solution efficiency of the approaches is carried out through a simulated model system, which is composed of four interconnected microgrids including EVs.

The remainder of this paper is organized as follows. Section 2 introduces the EVs charging load prediction method using BPNN and its correction approach based on LSTM. The multi-microgrid multi-objective energy management model is summarized in Section 3. Section 4 describes the solution method of the multi-objective scheduling problem. Section 5 shows the numerical examples with the predciton curve of EVs charging load and four connected microgrids system. Finally, Section 6 concludes the paper with a listing of major findings.

2. Day ahead electric vehicle charging load forecasting model

It is noted that the charging efficiency of batteries decreases as the temperature decreases, which causes automatic control systems to extend the charging time and reduce the rate of load reduction. In addition, people usually charge their EVs at night, which makes the charging load in a given microgrid area highly dependent on the time period. In this paper, we consider that the EV charging load can be affected by two factors: the charging efficiency determined by ambient temperature and the real-time number of charging EVs determined according to people's living habits.

The historical temperature employed in the present study was obtained from a weather station in Xi An, Northwestern China, as shown in Fig. 1, where 03:00 a.m. is regarded as the zero point and the temporal resolution is 1 h. The EV charging load training data were obtained from the charging pile management system in Northwestern China over a 15-day period and subjected to normalization, as shown in Fig. 2.

2.1. Back propagation neural network

To avoid the inherent characteristics of traditional mathematical models, some data-driven prediction methods such as ANN models have been introduced. As the most widely used neural network, a BPNN consists of a multi-layer feedforward neural network trained according to the error back propagation algorithm. As such, the forecast process of a BPNN consists of a forward calculation and a reverse calculation process. In the forward propagation process, the input data are processed layer by layer from the input layer through the hidden layer to the output layer, as illustrated in Fig. 3. The state of each layer only affects the state of the next layer of neurons. During the reverse calculation process, the error signal is returned along the original connection path, and the error is minimized by modifying the weight of each neuron [32]. This process is continued until the desired output is obtained at the output layer.

In this paper, the input matrix $\vec{x} = \begin{bmatrix} x_1 & x_2 & \dots & x_p \\ t_1 & t_2 & \dots & t_p \end{bmatrix}^T$ includes the temperature data and clock date. The output vector is composed of n elements: $\vec{y} = [y_1 \ y_2 \ \dots \ y_n]^T$. The output of each neuron in the l -th layer is $h^l = [h_1^l \ h_2^l \ \dots \ h_{s_l}^l]$, where s_l is the number of neurons in the first layer. Accordingly, this yields the following:

$$y_i = \sum_{j=1}^{s_{l-1}} w_{ij}^l h_j^{l-1} + b_i^l \quad (1)$$

During the training process, the present study adopts the following sigmoid function as the activation function:

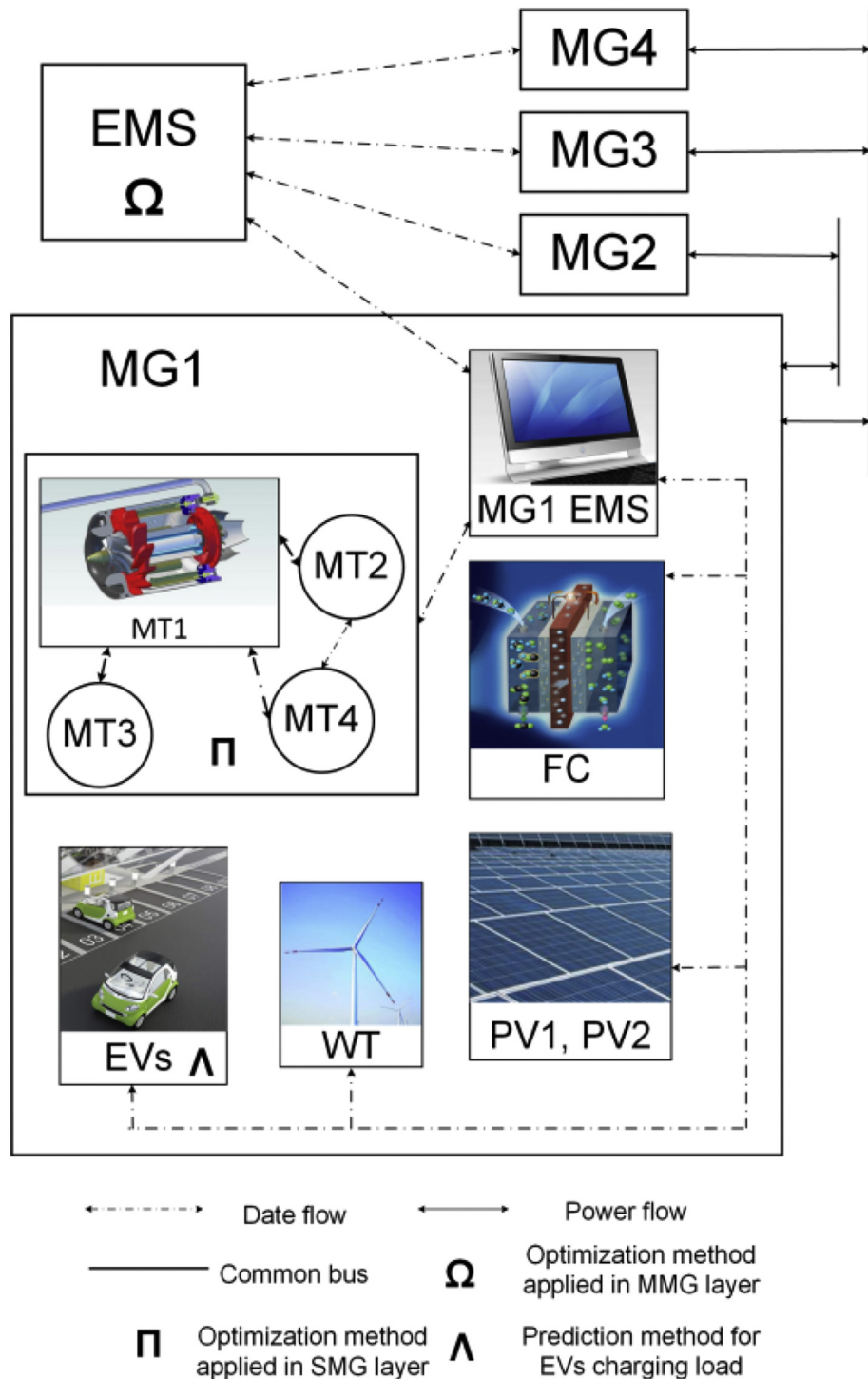


Fig. 1. Network topology of test multi-microgrid system.

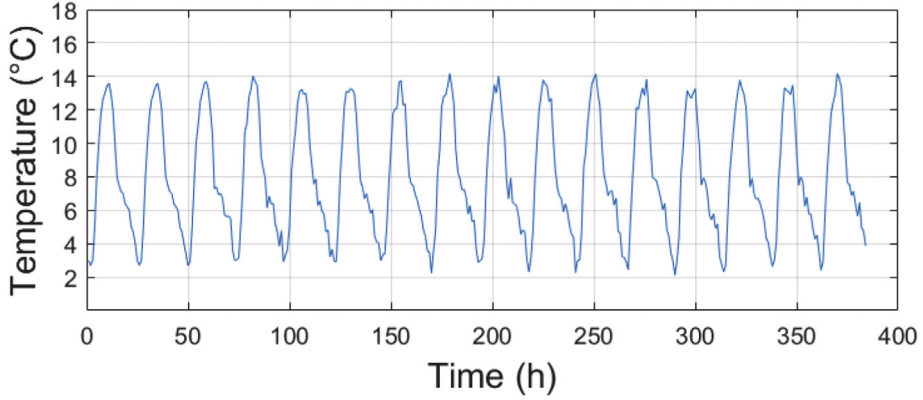


Fig. 2. Temperatures over 15-day period.

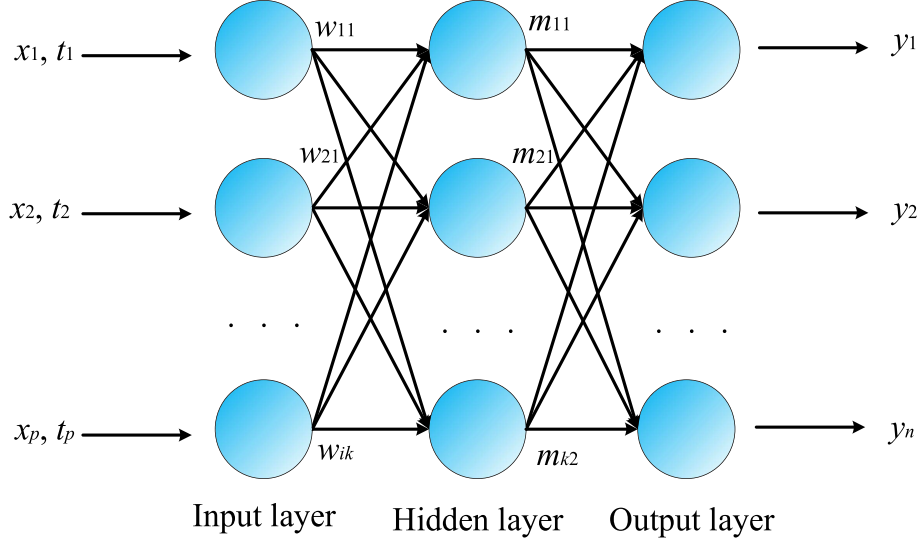


Fig. 3. Topology of BPNN.

$$f(x) = \frac{1 - e^{-x}}{1 + e^{-x}}$$

The error function is defined for the i -th training sample in the training sample set using the batch update method as follows:

$$\begin{cases} E = \frac{1}{N_{BP}} \sum_{i=1}^{N_{BP}} E(i) \\ E(i) = \frac{1}{2} \sum_{k=1}^n (d_k(i) - y_k(i))^2 \end{cases}$$

Accordingly, the following holds:

$$E = \frac{1}{2m} \sum_{i=1}^m \sum_{k=1}^n (d_k(i) - y_k(i))^2$$

Then, the weights and offsets are updated at each iteration according to the following formula:

$$\begin{cases} w_{ij}^l = w_{ij}^l - \alpha \frac{\partial E}{\partial w_{ij}^l} \\ b_i^l = b_i^l - \alpha \frac{\partial E}{\partial b_i^l} \end{cases}$$

Here, the range of the learning rate value is $(0, 1)$, and the partial derivatives of the output layer for a single training sample are given as follows:

$$\frac{\partial E(i)}{\partial w_{kj}^L} = -(d_k(i) - y_k(i)) f(x)'|_{x=n e_k^{(t)}} h_j^{L-1},$$

$$\frac{\partial E(i)}{\partial b_k^L} = -(d_k(i) - y_k(i)) f(x)'|_{x=n e_k^{(t)}}$$

Accordingly, the neural network training using the BPNN is conducted based on (1)–(7), and the obtained results of BPNN training are shown in Fig. 4. Details regarding the training process are shown in Fig. 5, consisting of the Gradient (the gradient of the error surface, when it reaches a set value, the training can be ended), the Mu (a variable that determines whether the training is done according to Newton's method or Gradient method), and the

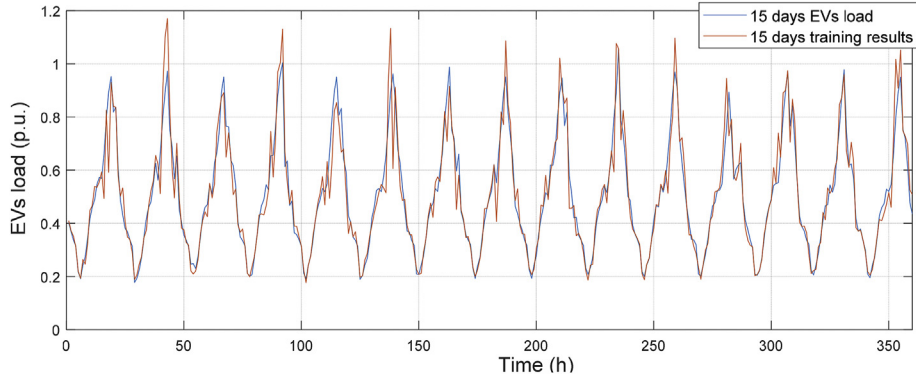


Fig. 4. Training data and results of BPNN training.

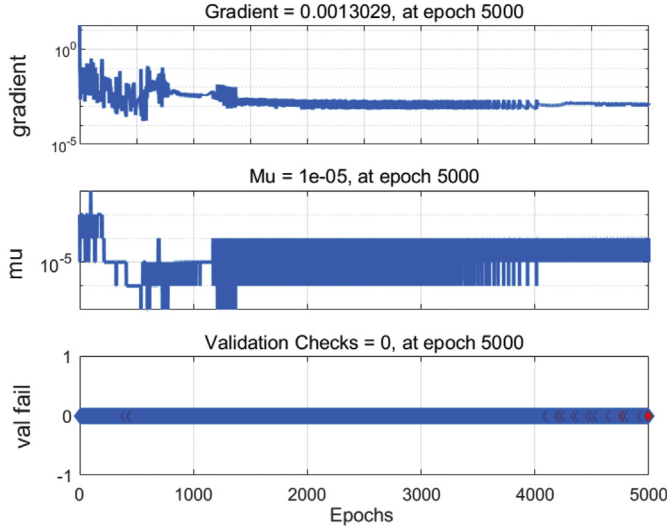


Fig. 5. Details regarding BPNN training process.

generalization ability check (if the training error does not decrease for six consecutive times, the training is forcibly terminated). In addition, we present the characteristics of convergence in Fig. 6 and the obtained prediction error in Fig. 7.

These results demonstrate that the weights minimizing the error can be obtained through multiple iterations and result in a good prediction outcome. However, while the convexity problem is solved by the partial derivative optimization method, it readily falls into a local optimal solution under conditions involving complex changes and influential factors. To address this problem, LSTM is introduced in this paper.

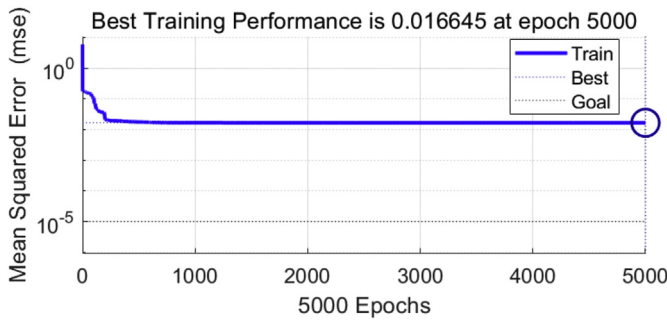


Fig. 6. Characteristics of BPNN training convergence.

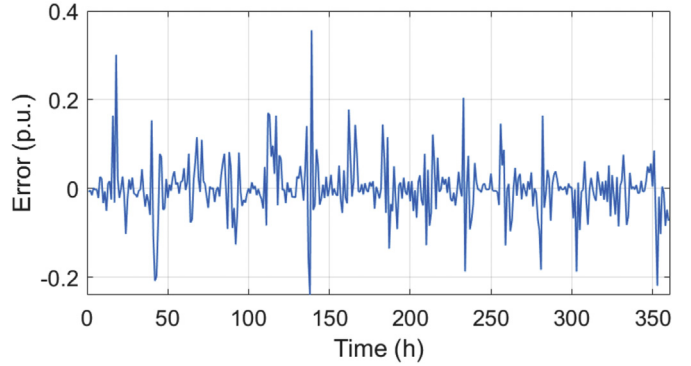


Fig. 7. Prediction error of trained BPNN.

2.2. Long short-term memory correction

It is noted that LSTM is a special type of recurrent neural network (RNN) designed to alleviate the problems of RNN use associated with long-term dependencies [33]. Here, prediction applications of classical RNN calculate the gradient in the form of the partial derivative products of activation functions [34]. If the partial derivatives of these activation functions are small (less than 1) or 0, the gradient readily vanishes over time. However, if the partial derivatives of these activation functions are large (greater than 1), the gradient will experience exponential growth. For long-term memory, which means that the relevant data have been subjected to multiple partial iteration calculations, the partial derivative may become extremely large or very small [35]. Fortunately, LSTM avoids long-term dependencies through the topography illustrated in Fig. 8 and has achieved superior results in distributed system optimization [36], information analysis [37], and image processing [38] applications.

In fact, the processing of LSTM includes four parts, namely input gate, forget gate, output gate, and cell state [39]. The specific features of these parts are listed in Appendix B. As the key to weaken the disappearance of the gradient, a suitable activation function is used to maintain the gradient within a reasonable range and an open gate does not completely replace the previous information, but introduces a weighted average between the previous information and the current information [40]. Therefore, the network will remember this information as long as the gate is open regardless of the depth of the network or the length of the input sequence.

In this paper, the learning mode of difference is proposed. Here, the 4th day in a sequence of 1-day periods (24 h) is first predicted at

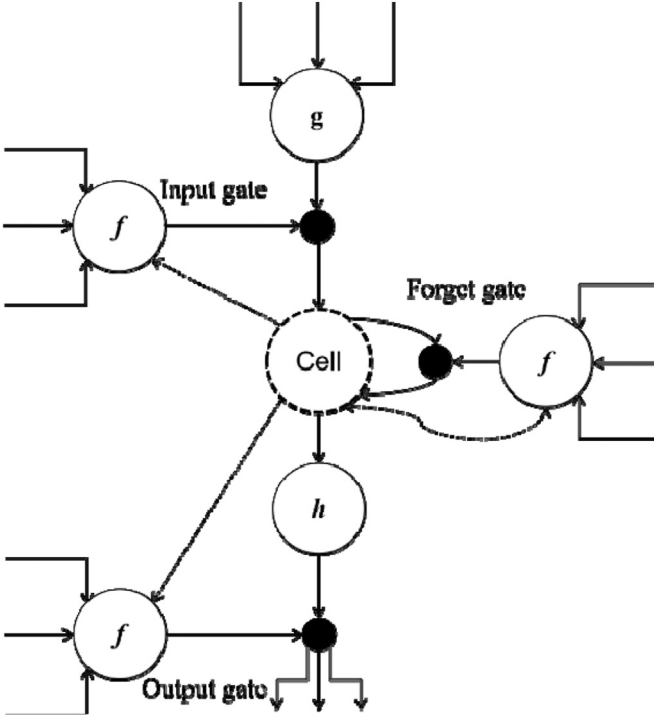


Fig. 8. Topology of LSTM cell.

each iteration based on the initial weights obtained using existing data over the first to third days (72 h). Then, the weights are corrected according to existing data for the 4th day. The corrected weights are then adopted to predict the data on the 5th day based on the existing data over the 2nd to the 4th days (72 h), and the weights are corrected according to existing data for the 5th day. This process continues up to the 15th day, resulting in a total of 11 sets of data. Finally, the data on the 16th day are predicted.

In the it -th iteration, the weights associated with the g -th group of data ($g = 1, 2, \dots, 11$) for the r -th hour ($r = 1, 2, \dots, 24$) are updated according to the following formula with the goal of minimizing the overall error. The main training equations are given in (8)–(11), and the weight conversion process of intermediate variables is shown in Appendix B.

$$\begin{cases} \min ER_{\text{tol}}^{it} = \sum_{j=1}^T |ER_j^{it}| \\ ER_j^{it} = H_{g,j}^{it} - D_{g,j} \\ H_{g,j}^{it} = \sum_{s=1}^{N_h} \tanh(C_{g,s}^{it}) \cdot o_{g,j}^{it} \cdot w_{s,g}^{it} \\ C_{j,g}^{it} = i_{g,j}^{it} \cdot G_j^{it} + C_{g-1,1}^{it} f_{g,j}^{it} \\ G_j^{it} = \tanh \left(\sum_{d=1}^{N_{\text{in}}} L_{g,j}^{\text{train}} \cdot w_{ix,d,j}^{it} + \sum_{e=1}^{N_{\text{out}}} H_{g-1,j}^{it} \cdot w_{ih,e,j}^{it} \right) \end{cases} \quad (8)$$

The gate matrices are defined as follows.

$$\begin{cases} i_{g,v}^{it} = 1 / (1 + e^{-ig_{g,v}^{it}}) \\ f_{g,v}^{it} = 1 / (1 + e^{-fg_{g,v}^{it}}) \\ o_{g,v}^{it} = 1 / (1 + e^{-og_{g,v}^{it}}) \end{cases} \quad (9)$$

Here, the output vector of the input gate, forget gate, and output gate are defined as follows.

$$\begin{cases} ig_j^{it} = \sum_{d=1}^{N_{\text{in}}} L_{g,j}^{\text{train}} \cdot w_{igx,d,j}^{it} + \sum_{e=1}^{N_{\text{out}}} C_{g-1,j}^{it} \cdot w_{ig,e,j}^{it} + b_{ig,j} \\ fg_j^{it} = \sum_{d=1}^{N_{\text{in}}} L_{g,j}^{\text{train}} \cdot w_{fgx,d,j}^{it} + \sum_{e=1}^{N_{\text{out}}} C_{g-1,j}^{it} \cdot w_{fg,e,j}^{it} + b_{fg,j} \\ og_j^{it} = \sum_{d=1}^{N_{\text{in}}} L_{g,j}^{\text{train}} \cdot w_{ogx,d,j}^{it} + \sum_{e=1}^{N_{\text{out}}} C_{g-1,j}^{it} \cdot w_{og,e,j}^{it} + b_{og,j} \end{cases} \quad (10)$$

The weights and their intermediate variables are updated according to the following formula.

$$\begin{cases} w_{ogx,i,r}^{it} = w_{ogx,i,r}^{it-1} - 2 \cdot \theta \cdot D_{ogx,i,r}^{it} \\ D_{ogx,i,j,r}^{it} = w_{ph,j,r}^{it-1} \cdot ER_r^{it-1} \cdot \tanh(C_{r,g}^{it-1}) \cdot e^{-og_j^{it-1}} \\ (og_j^{it-1})^2 \cdot L_{i,g}^{\text{train}} \\ w_{igx,i,r}^{it} = w_{igx,i,r}^{it-1} - 2 \cdot \theta \cdot D_{igx,i,r}^{it} \\ D_{igx,i,j,r}^{it} = w_{ph,j,r}^{it-1} \cdot ER_r^{it-1} \cdot og_j^{it-1} \cdot (1 - \tanh(C_{g,j}^{it-1})^2) \\ G_j^{it-1} \cdot e^{-ig_j^{it-1}} \cdot (ig_j^{it-1})^2 \cdot L_{i,g}^{\text{train}} \end{cases} \quad (11)$$

2.3. Two-layer combined back propagation neural network with long short-term memory correction

In summary, the main steps of the proposed two-layer prediction method can be given as follows.

1. Begin training with the BPNN based on the first 15 days of data, and obtain error data associated with the first 15 days.
2. Use the trained BPNN to predict the EV charging load on the 16th day, which is denoted as load L1.
3. Use LSTM to predict the EV charging load L2 on day 16 based on the first 15 days of data.
4. Based on the error data obtained in step 1, use LSTM to predict the error data w_{ER} for the data predicted on the 16th day by the BPNN, and obtain new load data L3 by conducting the correction as $L3 = w_{\text{ER}} + L1$.

3. Modeling of multi-objective energy management in a multi-microgrid system

The charging load of EVs can be obtained according to the methods presented in Section 2, and this is passed to the multi-objective optimization model.

3.1. Multi-microgrid modeling

In contrast to single-objective optimization problems, multi-objective problems typically involve conflicts between targets, so it is difficult to obtain a single solution where all the objective functions are optimal simultaneously. Therefore, the process typically provides a set of solutions that are inferior to the optimal solutions of the individual objective functions, and where the value of no objective function can be improved without weakening the value of at least one other objective function. This solution is called a non-dominated solution or Pareto optimal solution [41]. The operation structure of MG1 is illustrated in Fig. 1 as a typical SMG,

along with the specific network topology between microgrids.

The objectives presented in this paper include the network line loss, operating cost, and carbon emission. The multi-microgrid must meet its own load requirements during the scheduling period, and makes the network line loss, operation cost, and carbon emission be at a minimum. The functions associated with these objectives are presented as follows.

1) Network line loss

The network line loss of a multiple microgrid system at period t can be expressed by node admittance matrix \mathbf{G}_n as follows:

$$\min P_{\text{loss}}^t \sum_{i=1}^{N_n} \sum_{j \in i} u_i^t u_j^t \operatorname{re}(G_{n,ij}) \cos \delta_{ij}^t \quad (12)$$

2) Operating costs

The objective function for the total operating cost F of a multi-microgrid system is given as follows:

$$\min C = C_{\text{MT}} + C_{\text{FC}} + C_{\text{PV}} + C_{\text{WT}} \quad (13)$$

The specific costs are given as follows.

Diesel engines: The operating cost C_{MT} of diesel engines at period t can be approximated by a quadratic curve and is given as follows [42]:

$$C_{\text{MT}}^t = \sum_{j=1}^{N_{\text{MGS}}} \sum_{k=1}^{N_{\text{MT}}} a_{j,k} \left(P_{\text{MT},j,k}^t \right)^2 + b_{j,k} P_{\text{MT},j,k}^t + c_{j,k} + e_{j,k} \left| \sin \left(f \left(P_{\text{MT},j,k}^t - P_{\text{MT},j,k}^{\min} \right) \right) \right|. \quad (14)$$

Fuel cells: The operating cost C_{FC} of fuel cells at period t can be expressed as follows:

$$C_{\text{FC}}^t = \sum_{j=1}^{N_{\text{MGS}}} \sum_{k=1}^{N_{\text{MT}}} \left[C_{\text{CH4}} \frac{P_{\text{FC},j,k}^t}{\eta_{\text{FC}} \times L_{\text{HVNG}}} + K_{\text{FC},j,k} P_{\text{FC},j,k}^t \right]. \quad (15)$$

Renewable energy sources:

Since RESs consume no fuel, the operating cost of RESs, including those of WTs (C_{WT}) and PV units (C_{PV}), involves only maintenance costs and power generation costs [43]. Here, these costs are generally considered to have a linear relationship with respect to the active output. Therefore, C_{WT} and C_{PV} are given as follows:

$$\begin{cases} C_{\text{WT}} = \sum_{j=1}^{N_{\text{WT}}} P_{\text{WT},j} k_{\text{WT},j} \\ C_{\text{PV}} = \sum_{j=1}^{N_{\text{PV}}} P_{\text{PV},j} k_{\text{PV},j} \end{cases} \quad (16)$$

3) Carbon emissions

According to the operating data of thermal power units, the carbon emissions of a single MT and FC can be described as follows:

$$f_{\text{F,P}} = \sum_{t=1}^T \sum_{i=1}^{N_{\text{MT}}} g_{\text{MT},i} P_{\text{MT},i}^t + \sum_{t=1}^T \sum_{i=1}^{N_{\text{FC}}} g_{\text{FC},i} P_{\text{FC},i}^t \quad (17)$$

It is noted that the main pollutant emissions of thermal power units are carbon dioxide CO_2 , sulfur dioxide SO_2 , and nitrogen oxides NO_x . Because the emission of CO_2 is highly correlated positively with emissions of other pollutants and is regarded as the most widely used energy pollutant emission index, only CO_2 emissions are considered in this paper.

3.2. Constraints of multi-objective optimization

The operating constraints of the multi-microgrid system presented in this paper include the scheduling layer constraints between microgrids and the scheduling layer constraints in a single microgrid.

3.2.1. Scheduling layer constraints between microgrids

1) Power flow constraints

The power flow constraints are defined as follows for each branch of the network.

$$\begin{cases} \sum_{i:i \rightarrow j} \left(P_{ij} - R_{ij} I_{ij}^2 \right) - P_j = \sum_{l:j \rightarrow l} P_{jl} \\ \sum_{i:i \rightarrow j} \left(Q_{ij} - X_{ij} I_{ij}^2 \right) - Q_j = \sum_{l:j \rightarrow l} Q_{jl} \\ U_j^2 = U_i^2 - 2(R_{ij} P_{ij} + X_{ij} Q_{ij}) + (R_{ij}^2 + X_{ij}^2) I_{ij}^2 \end{cases} \quad (18)$$

$$I_{ij}^2 = \frac{P_{ij}^2 + Q_{ij}^2}{U_i^2} \quad (19)$$

In addition, the following constraints are applied for each node i ($i = 1, 2, \dots, n$) in the network.

$$\begin{cases} V_{i,\min} \leq V_i \leq V_{i,\max} \\ P_{G,i,\min} \leq P_{G,i} \leq P_{G,i,\max} \\ Q_{G,i,\min} \leq Q_{G,i} \leq Q_{G,i,\max} \\ |\delta_i - \delta_j| < |\delta_i - \delta_j|_{\max} \end{cases} \quad (20)$$

3.2.2. Scheduling layer constraints in a single microgrid

1) Electrical balance constraints

The electrical balance constraints between generation and demand are defined as follows:

$$P_{\text{load}}^t = P_{\text{MT}}^t + P_{\text{FC}}^t + P_{\text{WT}}^t + P_{\text{PV}}^t + P_{\text{trans}}^t. \quad (21)$$

2) Equipment balance constraints

The equipment balance constraints for mechanical outputs are defined as follows.

$$\left\{ \begin{array}{l} P_{MT,min,i} \leq P_{MT,i}^t \leq P_{MT,max,i} \\ P_{FC,min,i} \leq P_{FC,i}^t \leq P_{FC,max,i} \\ 0 \leq P_{wt,i}^t \leq P_{wt,i}^{t'} \\ 0 \leq P_{pv,i}^t \leq P_{pv,i}^{t'} \end{array} \right. \quad (22)$$

Meanwhile, those reflecting limits to equipment ramp rates are defined as follows.

$$\left\{ \begin{array}{l} P_{MT,d,max,i} \leq P_{MT,i}^{t+1} - P_{MT,i}^t \leq P_{MT,u,max,i} \\ P_{FC,d,max,i} \leq P_{FC,i}^{t+1} - P_{FC,i}^t \leq P_{FC,u,max,i} \end{array} \right. \quad (23)$$

4. Double layer energy management solution

The calculation time and convergence performance of the multi-objective energy management for multi-microgrids are enhanced by dividing the optimization model into two layers, where the upper optimization variables are the outputs of FCs, WTs and PVs in each microgrid, and the lower layer variables are the outputs of MTs.

Firstly, with the purpose of minimizing C_{MT} , the power outputs of MTs are distributed using the CA:

$$\min C_{MT,j} = \sum_{k=1}^{N_{MT}^j} a_{j,k} (P_{MT,j,k})^2 + b_{j,k} P_{MT,j,k} + c_{j,k} + e_{j,k} |\sin(f(P_{MT,j,k} - P_{MT,j,k}^{\min}))|. \quad (24)$$

However, the existence of the valve point effect $e_{j,k} |\sin(f(P_{MT,j,k} - P_{MT,j,k}^{\min}))|$ makes it impossible for conducting optimization using CA directly. This problem is addressed here by limiting the valve point effect within an acceptable error range using a multi-model approximation method.

4.1. Multi-model approximation method

Taking an MT in the j -th microgrid as an example, the specific multi-model approximation process is given as follows.

1. Obtain the cost curve C_{1j} considering the valve point effect, the cost curve C_{2j} not considering the valve point effect, and their intersections $\mathbf{x}_1, \mathbf{x}_2, \dots, \mathbf{x}_n$ according to the output characteristics of the MT unit.
2. According to the intersection points, the cost curve C_{1j} is divided into $n - 1$ intervals $[\mathbf{x}_1, \mathbf{x}_2], [\mathbf{x}_2, \mathbf{x}_3], \dots, [\mathbf{x}_{n-1}, \mathbf{x}_n]$.
3. Then, representative points of each interval i ($i = 1, 2, \dots, n - 1$) shown in Figs. A1–A4 are obtained through MPC, MP, and ZPSD, respectively. And the specific steps of these methods are presented in Appendix C.
4. Perform a quadratic fitting to the representative point set obtained for curve C_{1j} . This yields three approximate curves $C_{MPC,j}$, $C_{MP,j}$, and $C_{ZPSD,j}$. The error rates of these curves are then respectively calculated as follows:

$$\left\{ \begin{array}{l} er_{MPC,j} = \sum_{k=1}^{N_{MT}^j} \int_{P_{MT,j,k}^{\min}}^{P_{MT,j,k}^{\max}} |C_{MPC,j} - C_{1j}| dx \\ er_{MP,j} = \sum_{k=1}^{N_{MT}^j} \int_{P_{MT,j,k}^{\min}}^{P_{MT,j,k}^{\max}} |C_{MP,j} - C_{1j}| dx \\ er_{ZPSD,j} = \sum_{k=1}^{N_{MT}^j} \int_{P_{MT,j,k}^{\min}}^{P_{MT,j,k}^{\max}} |C_{ZPSD,j} - C_{1j}| dx \end{array} \right. \quad (25)$$

The representative points obtained by the method with the smallest error are then selected.

5. Repeat steps 1–4 for the remaining microgrids.

This process facilitates the rapid output dispatch of multiple units using CA. Compared with traditional methods, the number of the control variables is reduced by $\sum_{j=1}^{N_{MG}} N_{MT}^j - N_{MG}$, which improves the performance of computational cost.

4.2. Energy management of single microgrid based on consistency theory

The application in peer-to-peer (P2P) environment [42] reflects CA's ability of dynamically allocating resources, which can be well adapted to the microgrid energy management problem. It's used to describe the interaction between agents in a multi-agent system, also known as a coherence protocol. The CA of the entire system can be expressed by the following matrix expression:

$$\mathbf{AG}_{n+1} = \mathbf{H} \bullet \mathbf{AG}_n, \quad (26)$$

where $\mathbf{H} = I - \theta \mathbf{L}$, \mathbf{H} is an n -order non-negative matrix, I is an N -order unit matrix, and \mathbf{L} is the Laplacian matrix of the communication topology of the microgrid. If \mathbf{H} is a non-negative row random matrix and all eigenvalues are not greater than 1, then all the agents of the system will converge to the same value after a sufficient number of iterations [43].

The consistency variable employed in this paper is the incremental discharge $r_{j,k}$ of each unit k in each microgrid j . Each agent unit in the distributed optimal energy management strategy requires only information from a neighboring agent, making the solution method capable of easily adjusting the system structure change by changing a few elements of \mathbf{H} . This yields the following relationship:

$$r_{j,k} = a_{j,k} P_{MT,j,k} + b_{j,k} \quad (27)$$

The parameters of each agent in microgrid j are subject to iteration according to the following formula:

$$\left\{ \begin{array}{l} r_{j,k}^{n+1} = \sum_{g \in N_i^+} h_{j,k,g} r_g^n + \varepsilon \cdot P_{L,j,k}^n \\ P_{MT,j,k}^{n+1} = \frac{r_{j,k}^n - b_{j,k}}{a_{j,k}} \\ P_{L,j,k}^{n+1} = \sum_{g \in N_{nb,i}^+} v_{j,k,g} P_{L,g}^n - (P_{MT,j,k}^{n+1} - P_{MT,j,k}^n) \end{array} \right. \quad (28)$$

Here, the communication network parameter h_{ij} is an element of

\mathbf{H} , where \mathbf{H} is ensured to be a non-negative row random matrix due to the particularity of the grid communication structure. For example, if agent i is not connected to agent j , $h_{ij} = 0$, and if agent i is connected to agent $j = 1, 2, \dots, k$, then $h_{ij} = \frac{1}{k}$. Furthermore, the communication network parameter v_{ij} is an element of a non-negative column random matrix \mathbf{V} . Considering that all MTs are agents, the output of MTs in single microgrid layer can be obtained. And the specific steps of establishing the output of MT unit k of microgrid j using CA are listed in Appendix D.

4.3. Multi-objective energy management of multiple microgrid based on improved MOEA/D

The application of multi-objective evolutionary algorithm based on decomposition (MOEA/D) in unit planning [44] and voltage control [45] reflects its optimal solution searching ability in multi-objective problems. The control variables of MOEA/D employed in the present work for multi-objective energy management in the multi-microgrid layer are WT, PV, and FC outputs in each microgrid, and the power transmitted to or from each microgrid, which is positive when the microgrid outputs power and is negative when power is injected into the microgrid from an external microgrid.

The MOEA/D is based on the Tchebycheff framework [46], which decomposes a multi-objective problem into a set of scalar optimization subproblems and then optimizes all subproblems simultaneously in one single iteration. During initialization, the population size of the solution is set to N_{POP} , m objective functions are considered, and the domain size is set to T .

Set reference point $Z^* = (Z_1^*, \dots, Z_m^*)^T$, and define $\lambda = \begin{bmatrix} \lambda_{1,1} & \lambda_{1,2} & \dots & \lambda_{1,m} \\ \lambda_{2,1} & \lambda_{2,2} & \dots & \lambda_{2,m} \\ \vdots & \vdots & & \vdots \\ \lambda_{N,1} & \lambda_{N,2} & \dots & \lambda_{N,m} \end{bmatrix}$ as a set of uniformly distributed

weight vectors. The Tchebycheff method transforms the problem of solving the Pareto frontier into a series of scalar problems, and the objective function of the j -th ($j = 1, \dots, N$) subproblem is

$$g(x, \lambda^j, z^*) = \min\{\lambda_{i,j}|f_i(x) - z_i^*|\}, \quad 1 \leq i \leq m \quad (29)$$

In MOEA/D, the neighborhood of a weight vector is defined as the set of several of its nearest weight vectors R . Therefore, the neighborhood of the j -th subproblem includes the weight vectors of all subproblems from the neighborhood of the elements $\lambda_{j,i}$, $1 \leq i \leq m$ in matrix λ . The population is made up of the best solutions thus far obtained for each subproblem. In this paper, the evolutionary operator selection mechanism uses the integral system to improve the distributability and global search ability of the Pareto solution set. These include the following imitation binary crossover operator (SBX):

$$\begin{cases} V_{1j}(t) = 0.5 \times [(1 + \gamma_j)X_{1j}(t) + (1 - \gamma_j)X_{2j}(t)] \\ V_{2j}(t) = 0.5 \times [(1 - \gamma_j)X_{1j}(t) + (1 + \gamma_j)X_{2j}(t)] \end{cases} \quad (30)$$

$$\gamma_j = \begin{cases} (2u_j)^{\frac{1}{\eta+1}}, & u_j \leq 0.5 \\ \left(\frac{1}{2(1-u_j)}\right)^{\frac{1}{\eta+1}}, & \text{otherwise} \end{cases} \quad (31)$$

In addition, differential evolution theory includes five evolutionary operators: DE/rand/1, DE/best/1, DE/rand to best/1, DE/best/2, and DE/rand/2, which are, respectively, defined as follows.

$$\begin{cases} V_i(g) = X_{p1}(g) + F \cdot (X_{p2}(g) - X_{p3}(g)) \\ V_i(g) = X_{best}(g) + F \cdot (X_{p1}(g) - X_{p2}(g)) \\ V_i(g) = X_i(g) + F \cdot (X_{best}(g) - X_i(g)) + F \cdot (X_{p1}(g) - X_{p2}(g)) \\ V_i(g) = X_{best}(g) + F \cdot (X_{p1}(g) - X_{p2}(g)) + F \cdot (X_{p3}(g) - X_{p4}(g)) \\ V_i(g) = X_{p1}(g) + F \cdot (X_{p2}(g) - X_{p3}(g)) + F \cdot (X_{p4}(g) - X_{p5}(g)) \end{cases} \quad (32)$$

The population consists of six sub-populations with an initial size ($N_{POP}/6$), and each sub-population is associated by the above six evolutionary operators. The number of non-dominated solutions $N_{d,1} - N_{d,6}$ of each lower layer is counted every three iterations, and the evolution operator probability $P_{JP,i}$ in the next three iterations is determined for each individual according to the following formula:

$$P_{JP,i} = \frac{N_{d,i} e^{1 - \frac{n}{n_{max}}}}{N \sum_{i=1}^6 N_{d,i}} \quad (33)$$

The specific steps for conducting multi-objective energy management of a multi-microgrid system based on the improved MOEA/D, named the multi-objective evolutionary algorithm based on decomposition-adaptive multi-model (MOEA/D-AMM), are given as follows.

- (1) Initialize the population as $N_{POP}/6$, the number of objective functions as $m = 3$, the neighborhood size as T , and reference point Z^* as $(0,0,0)$.
- (2) Calculate the Euclidean distance between any two weight vectors, and calculate the T weight vectors nearest to each weight vector. For $i = 1, \dots, N_{POP}$, set $B(i) = \{i1, \dots, iT\}$, where $\lambda_{j,i}, 1 \leq i \leq T$ are the T weight vectors closest to λ_j .
- (3) Generate an initial population randomly or through some method specific to the problem. Then, calculate the objective function vector $F_i = [f_1(x_i), \dots, f_m(x_i)]$ for each individual in the population, and select the non-dominated solution set EP from the initialized weight vectors.
- (4) Individual x_i , $i = 1, \dots, N_{POP}$ is mutated using the six evolutionary operators in (44) and (45) according to the corresponding mutation probability $P_{JP,i}$.
- (5) If $z_j > f_j(y_i)$ for all $j = 1, \dots, m$, then set $z_j = f_j(y_i)$.
- (6) For $j \in B(i)$, set $x_i = y_i$ and $F_i = F(y_i)$ if $g(y, \lambda_j, z) \leq g(x_i, \lambda_j, z)$.
- (7) Remove all solutions that are dominated by $F(y_i)$ from EP. If no solution in EP dominates $F(y_i)$, then $F(y_i)$ is added to EP.
- (8) If the stop criterion is met, stop and output EP. Otherwise, return to step 4.

A flowchart of the proposed load prediction method and multi-objective energy management model of multi-microgrids is shown in Fig. 9.

5. Case study

5.1. Test multi-microgrid system description and case study framework

As illustrate in Fig. 1, a multi-microgrid system consisting of two IEEE 9-node systems MG1 and MG2 and two IEEE 14-node systems MG3 and MG4 is employed as a case study to verify the performance of the proposed model. The network information for the multi-microgrid system, the network information for the individual microgrids, and the buses at which individual energy resources are

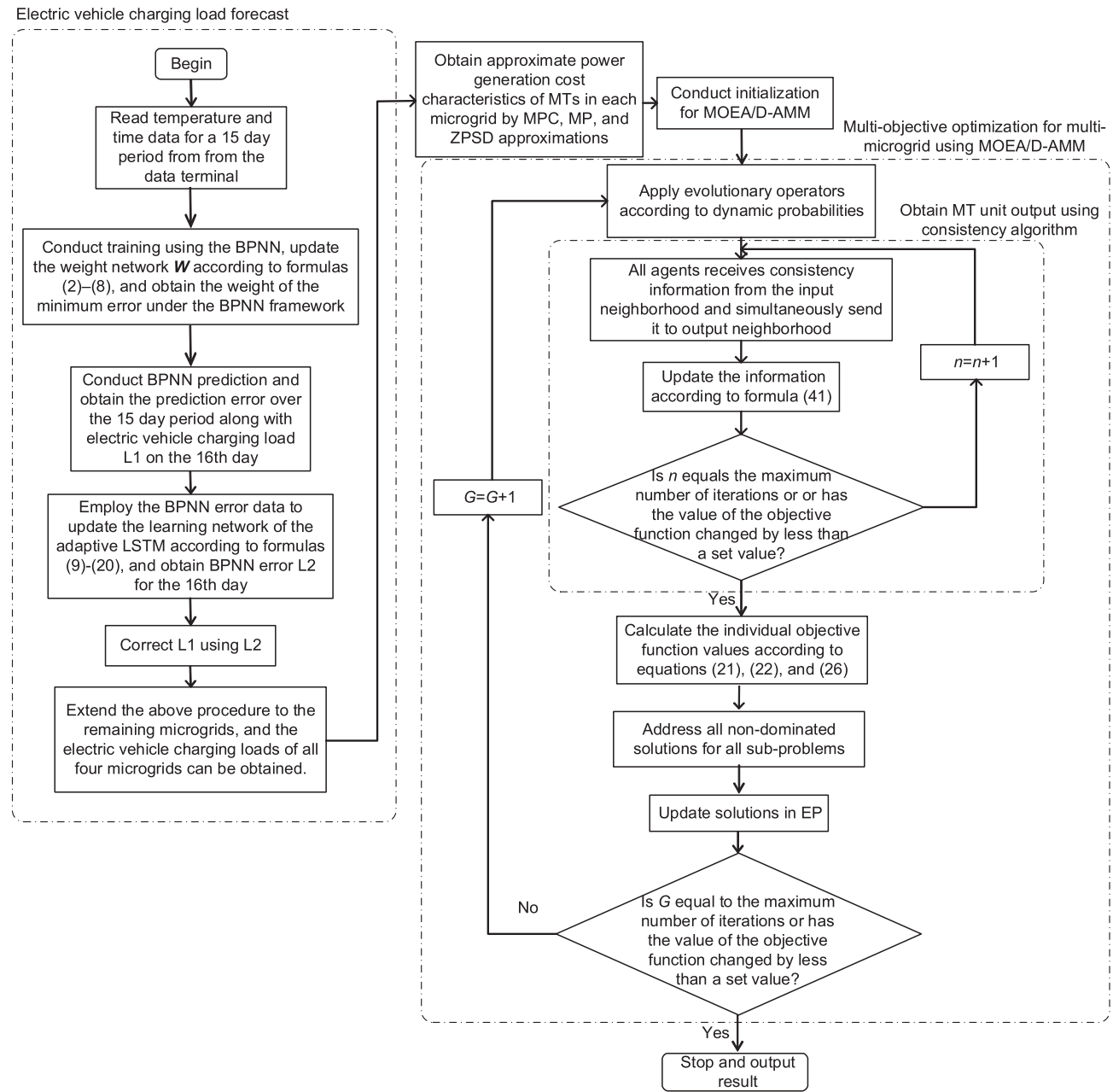


Fig. 9. Flowchart of presented electric vehicle load forecasts method and proposed multi-objective optimization algorithm.

installed are listed in **Tables 1–3**, respectively.

Here, the iteration limits of the conventional MOEA/D and proposed MOEA/D-AMM algorithms are 50, the population sizes are 300, and the maximum power of the transmission lines is 6 MW. The predicted active loads, PV unit outputs, and WT outputs of the four microgrids obtained by BPNN and historical data given

Table 2
Network information for four microgrids in test system.

	MG1	MG2	MG3	MG4
Node number	9	14	14	9
WT number	1	0	1	0
PV number	2	1	3	1
FC number	1	1	1	1
MT number	4	5	5	3

Table 1
Network information for test multi-microgrid system.

Line	From bus	To bus	R (Ω)	X (Ω)
1	1	3	0.04	0.25
2	1	2	0.1	0.35
3	1	4	0.08	0.3
4	3	4	0.06	0.4

by local systems are shown in **Fig. 10**. All numerical computations were conducted on a personal computer with a 4-core 2.6 GHz CPU and 4 GB of memory running Windows 10. The EV charging load prediction and the overall multi-objective optimization model were established using MATLAB.

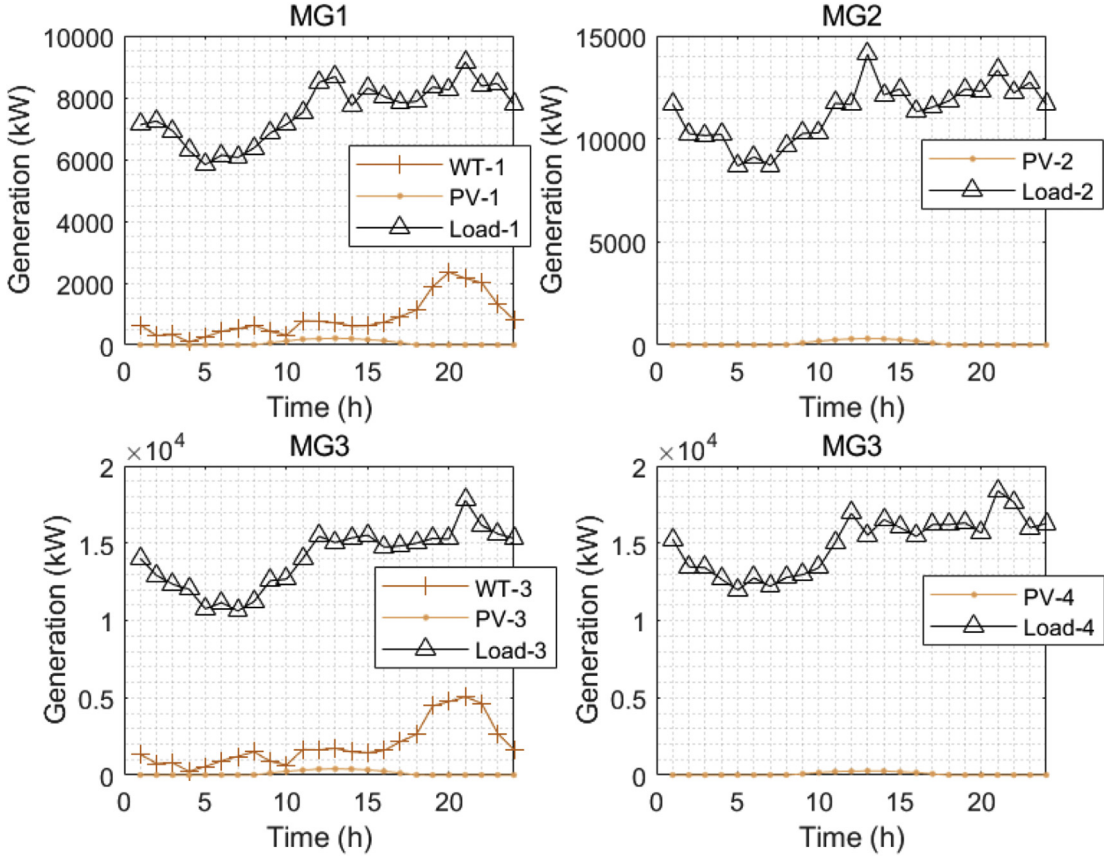


Fig. 10. Active loads and outputs of renewable energy sources for four test microgrids.

5.2. Electric vehicle charging load prediction

The results of the improved EV charging load prediction method are illustrated in Figs. 11–14 for MG1 over the 24 h period on the 16th day. In addition, the convergence performance of the adaptive LSTM is illustrated in Fig. 14.

Based on formula (4), we note that the total error of the predicted EV charging load value forecasted using the standard LSTM is 14.09% and that forecasted using the standard BPNN is 6.324%. However, we note from Fig. 13 that the error of the EV charging load predicted using the proposed BPNN-LSTM method is 3.995%, which reduced the error of the standard LSTM method by 71.68% and that of the standard BPNN method by 36.86%. The special forget gate

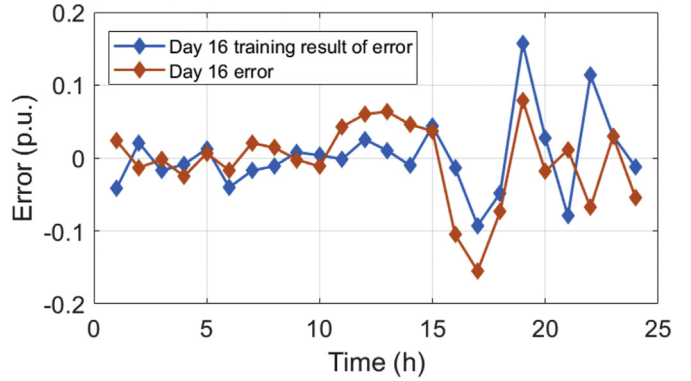


Fig. 12. Forecasting errors for MG1 obtained on day 16 using LSTM.

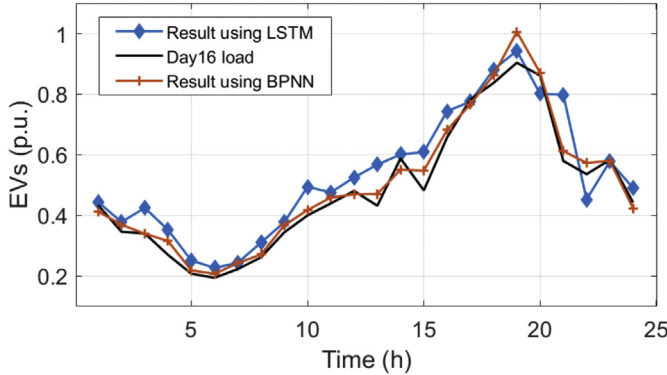


Fig. 11. EV charging load forecasts for MG1 obtained on day 16 using BPNN and LSTM.

structure and activation function of LSTM allows it to predict the error of the BPNN via long-term error data (i.e., 15 days), which effectively addresses the problem that the BPNN is prone to the loss of early data weights when applied to long-term prediction. The above method was then extended to the remaining three microgrids to obtain the EV charging loads of all four microgrids.

Prior to obtaining the solution of the multi-objective dispatch problem, the output curves of MTs are approximated based on (C1)–(C3) to ensure that CA is feasible. The approximation process is illustrated in Figs. A1–A4, and the errors are listed in Table 4.

The results indicate that the MP method yields the smallest error for MG1, while the MPC method yields the smallest errors for MG2, MG3, and MG4. Therefore, these approximation results were

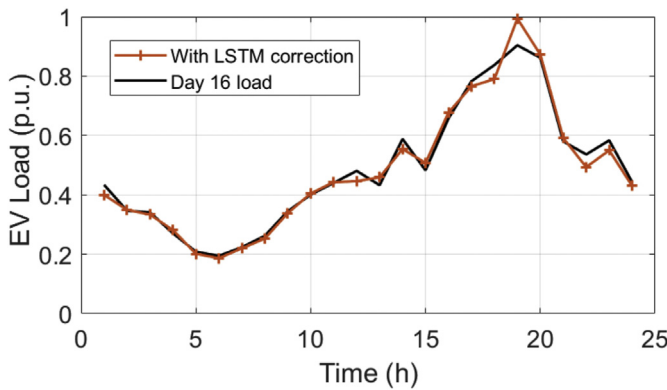


Fig. 13. EV charging load forecasts for MG1 obtained on day 16 after correction using adaptive LSTM-BPNN.

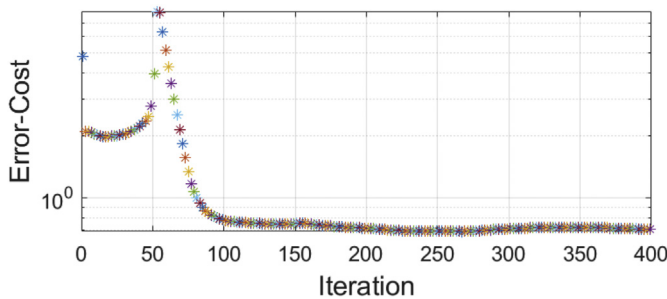


Fig. 14. Convergence performance of adaptive LSTM.

Table 3
Selected buses at which energy resources are installed.

Type	Location (bus)	Capacity (kW)
WT	1-2, 3-7	2500, 6000
PV	1-1, 2-1, 3-11, 4-5	300, 400, 450, 300
FC	1-7, 2-5, 3-4, 4-3	1500*4
MT	1-3, 1-4, 1-8, 1-6 2-3, 2-6, 2-8, 2-10, 2-13 3-1, 3-3, 3-5, 3-8, 3-13 4-1, 4-3, 4-4, 4-7	1500*4 2000*5 3000*5 6500*4
Trans-nodes	1-6, 2-2, 3-12, 4-2	4000

Table 4
Errors of various approximation methods of MT output curve for each microgrid in test system.

	MG1	MG2	MG3	MG4
MPC	1.481%	0.527%	0.2810%	0.331%
MP	1.383%	0.787%	1.131%	1.283%
ZPSD	5.317%	2.843%	4.156%	5.387%
NC	7.685%	3.301%	19.56%	5.885%

employed for testing the proposed multi-objective energy management scheme.

5.3. Comparison of the economic performance obtained by multi-objective dispatching algorithms

Firstly, with the single goal of minimizing operation cost, the conventional MOEA/D and MOEA/D-AMM algorithms are used to conduct multi-microgrid energy management over a 24 h scheduling period. The transmitted power P_{MG} of the four microgrids

obtained by the conventional MOEA/D and MOEA/D-AMM under the optimization condition of the minimum operating cost is shown in Figs. 15 and 17, respectively. In addition, the power outputs of controllable units in the four microgrids obtained by the conventional MOEA/D and MOEA/D-AMM algorithms are shown in Figs. 16 and 18, respectively.

It can be seen in Fig. 10 that the active loads of the four microgrids are low from 00:00 to 08:00, and Fig. 15 indicates that only MG1 and MG2 exhibit power shortages. However, all microgrids meet their load requirements from 08:00 to 11:00, and no additional power transmission is needed. From Fig. 15, we note that the need to minimize costs ensures that the MT units in MG1 and MG2 generally operate at a full capacity, and the FC unit outputs are only increased when the active load is high. In addition, the WT output of MG1 reached its maximum value only in the period 19:00–23:00 due to the local wind speed conditions. Finally, the cost of the multi-microgrid system is reduced during the peak load period by gradually increasing the MT output of MG4 and transmitting its generated power to the other microgrids because MG4 provides the lowest power generation cost.

Figs. 16 and 18 indicate that the solution provided by MOEA/D-AMM is similar to that provided by conventional MOEA/D, except that the power transmission between microgrids shown in Fig. 18 is more evenly balanced than that presented in Fig. 16. For example, the solutions provided by MOEA/D for MG1, MG2, and MG3 exhibit greater power shortages requiring compensation by MG4 in the period 12:00–23:00 than the solutions provided by MOEA/D-AMM. This indicates that the collaborative scheduling capability of the proposed MOEA/D-AMM algorithm is more effective for the test multi-microgrid system than that of conventional MOEA/D. In addition, according to the comparison of Figs. 17 and 19, it is found that both can provide a solution that satisfies the constraints. The solution provided by MOEA/D-AMM can provide more stable power output planning for MG3 and MG4 from 00:00 to 09:00, and can absorb more wind energy.

Finally, formulas (13)–(16) are applied to obtain the operating costs provided by conventional MOEA/D and the proposed MOEA/D-AMM algorithm, which were 188,578.34 yuan and 184,579.51 yuan, respectively, indicating that the improved algorithm reduced the cost by 2.2653%.

5.4. Comparison of pareto fronts obtained by multi-objective dispatching algorithms

The Pareto fronts obtained for the test multi-microgrid system at time period 13 using the conventional MOEA/D and MOEA/D-AMM algorithms under the three optimization conditions of minimum network loss, operation cost, and carbon emission were

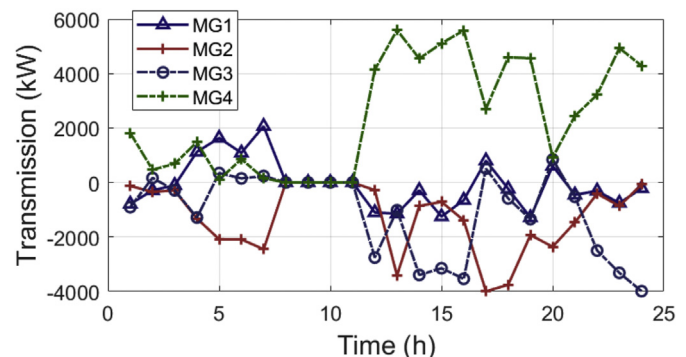


Fig. 15. Power transmitted solutions provided by conventional MOEA/D.

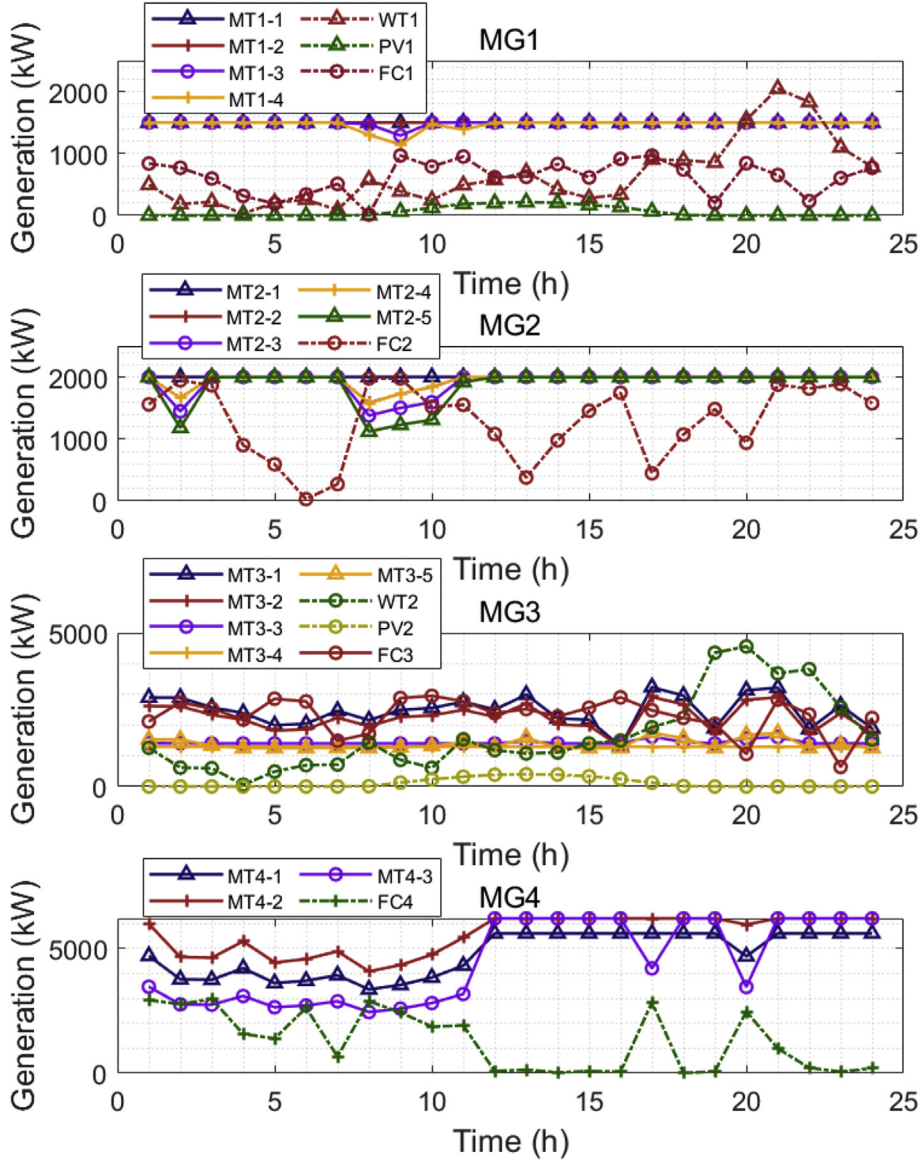


Fig. 16. Power generation solutions provided by conventional MOEA/D.

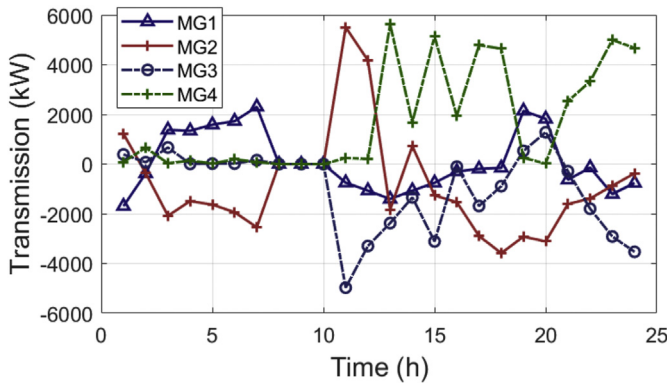


Fig. 17. Power transmitted solutions provided by proposed MOEA/D-AMM.

evaluated, and the results are presented in Figs. 19 and 20, respectively.

As a comparison, Fig. 19 indicates that conventional MOEA/D provides a minimum carbon emission of 41.44 kg for the test multi-microgrid system when the network loss is 0.01006 MW and the operating cost is 93,970 yuan. Meanwhile, Fig. 20 indicates that the proposed MOEA/D-AMM algorithm provides a minimum carbon emission of 40.74 kg for the test multi-microgrid system when the network loss is 0.01002 MW and the operating cost is 93,960 yuan. Accordingly, the improved algorithm achieves a 1.69% reduction in carbon emission when the values associated with the other two objectives are at the same level. Similarly, when carbon emission and operating cost provided by the two algorithms are at the same levels of 40.95 kg and 93,970 yuan, the network loss provided by the improved algorithm is 0.00788 MW while that provided by the conventional algorithm is 0.01385 MW, representing a 43.08% reduction. When carbon emission and network loss provided by the two algorithms are at the same levels of 39.44 kg and 0.0130 MW, the operating cost provided by the improved algorithm

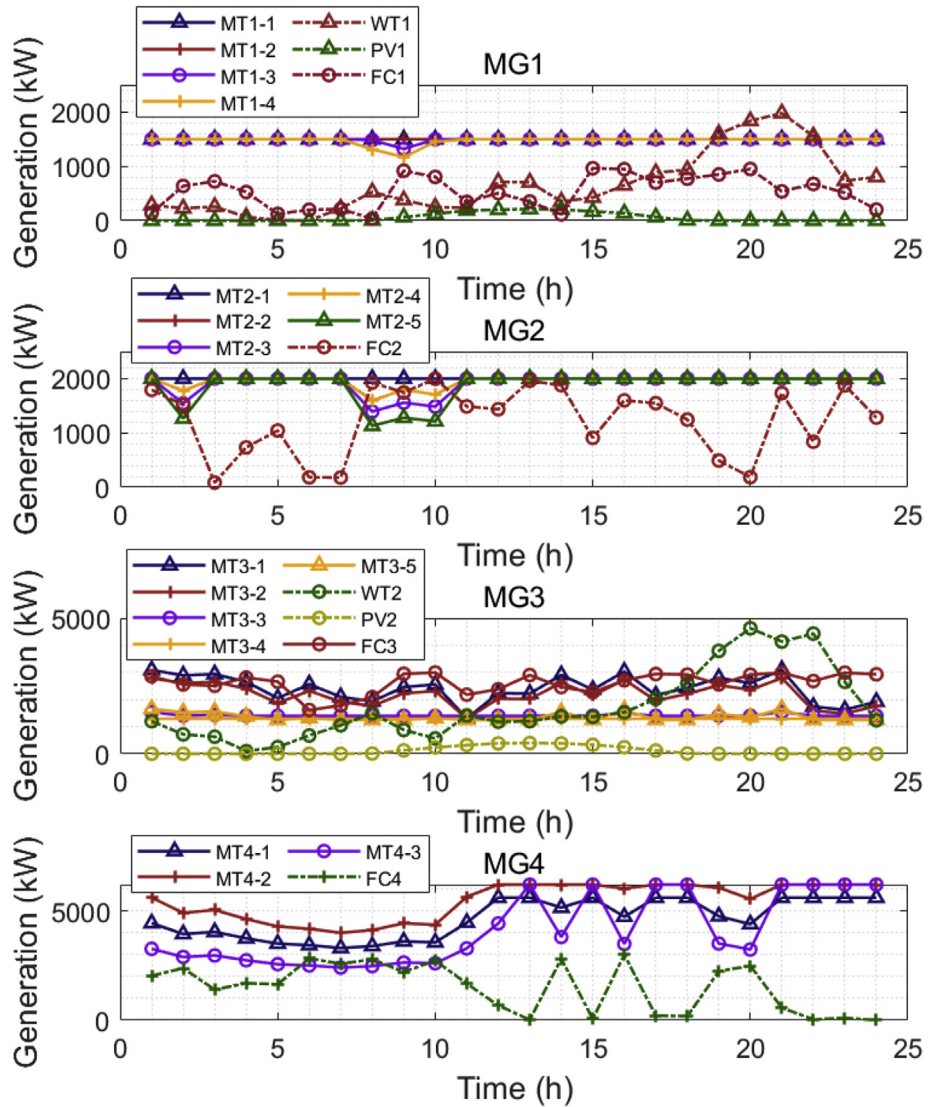


Fig. 18. Power generation solutions provided by proposed MOEA/D-AMM.

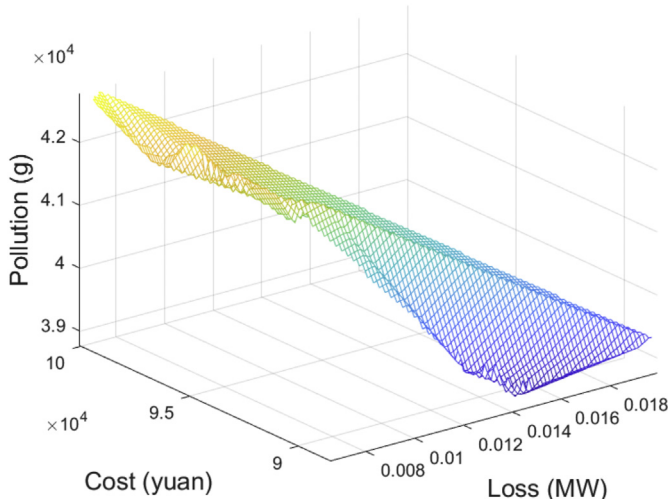


Fig. 19. Pareto front provided by conventional MOEA/D.

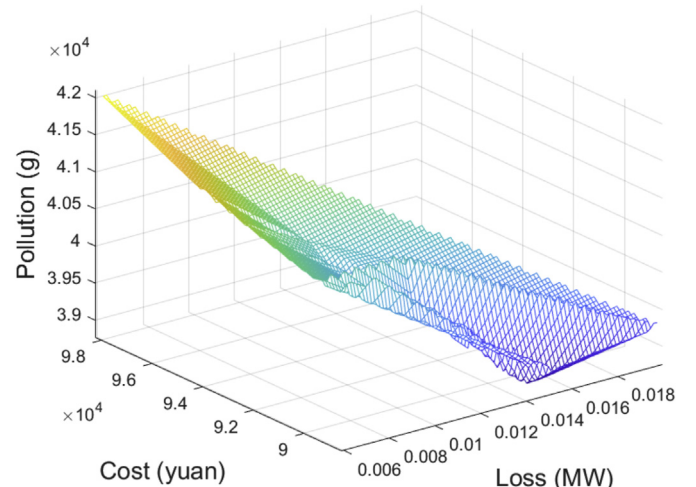


Fig. 20. Pareto front provided by proposed MOEA/D-AMM.

is 89,470 yuan while that provided by the conventional algorithm is 90,590 yuan, representing a 1.23% reduction. The discussion above indicates that MOEA/D-AMM offers a particularly significant advantage for reducing any one objective when the other two are maintained at the same levels.

It is also noted from a comparison of the shapes of the two Pareto fronts in Figs. 19 and 20 that the Pareto front provided by MOEA/D lies away from the ideal point (0, 0, 0) in the middle, while the Pareto front provided by MOEA/D-AMM has moved toward (0, 0, 0). These results indicate that MOEA/D-AMM provides a superior Pareto front than MOEA/D and therefore offers a better global optimal solution search capability for the three-objective optimization of the test multi-microgrid system.

In addition, it is noted that the application of DE in the upper layer can reduce the probability of falling into local optimal solutions through multi-dimensional variation, while the structure of the AMM will increase the time required for each iteration. As for the lower layer method, the CA can reduce the time required for each iteration. These features ensure a reasonable calculation time for the improved algorithm, which is verified in the following subsection.

5.5. Comparison of the convergence performance obtained by multi-objective economic dispatching algorithms

Here, the convergence process for each of the three objective functions is expressed more dynamically and clearly by considering five intervals of objective function values with respect to the number of iterations, where the intervals are divided according to the principle of 20% of data per interval. First, the values of objective function m obtained in the it iteration are sorted from largest to smallest as $[f_{m,1}^{it}, \dots, f_{m,N_{pop}}^{it}]$. Accordingly, the five intervals of values for objective function m can be defined as $[f_{m,1}^{it}, \dots, f_{m,\frac{N_{pop}}{5}}^{it}], [f_{m,\frac{N_{pop}}{5}+1}^{it}, \dots, f_{m,\frac{2*N_{pop}}{5}}^{it}], [f_{m,\frac{2*N_{pop}}{5}+1}^{it}, \dots, f_{m,\frac{3*N_{pop}}{5}}^{it}], [f_{m,\frac{3*N_{pop}}{5}+1}^{it}, \dots, f_{m,\frac{4*N_{pop}}{5}}^{it}],$ and $[f_{m,\frac{4*N_{pop}}{5}+1}^{it}, \dots, f_{m,N_{pop}}^{it}]$. The convergence processes of the objective function values provided by two algorithms are shown in Tables 5 and 6.

The specific convergence processes of the objective function values provided by the conventional MOEA/D and MOEA/D-AMM algorithms in each interval is shown in Figs. A5–A7 and A8–A10, respectively.

The specific convergence processes of the objective function values provided by the conventional MOEA/D and MOEA/D-AMM algorithms in each interval are shown in Figs. A5–A7 and A8–A10, respectively. According to the calculation results, the time required for 50 iterations using MOEA/D is 143.56 s, and stable convergence is obtained at the 43rd iteration. Therefore, the time required to reach stable convergence is 123.46 s. In contrast, the time required for 50 iterations using MOEA/D-AMM is 139.21 s, and stable convergence is achieved at the 25th iteration. Therefore, the time required to reach stable convergence is 69.61 s. This indicates that the proposed algorithm provides a significantly more rapid convergence for network loss than conventional MOEA/D.

In addition, the Shannon-Wiener index is introduced for further

comparison. This index represents a measurement of community diversity used in information theory and seeks to predict the type to which the next individual in the population belongs. Here, the uncertainty of the prediction increases with increasing community diversity [50]. Specifically, the index is calculated based on the proportion PG_i of the i -th interval PG_i in a collection of individuals as follows:

$$\left\{ \begin{array}{l} SW = - \sum_{i=1}^{i=5} PG_i (\ln(PG_i)) \\ PG_i = \frac{\frac{f_{(i+1)*N_{pop}}^{50} - f_{i*N_{pop}}^{50}}{5}}{f_{N_{pop}}^{50} - f_1^{50}} \end{array} \right. \quad (34)$$

Based on the data shown in Tables 5 and 6, the Shannon-Wiener index values obtained for the three objective functions are listed in Table 7. It can be seen that the MOEA/D-AMM algorithm provides Shannon-Wiener index values for objective function values 1, 2, and 3 that are, respectively, 8.68%, 13.82%, and 21.45% greater than those provided by conventional MOEA/D. These results indicate that the non-dominated solutions in the pareto set provided by MOEA/D-AMM distribute more uniformly.

6. Conclusion

Potential power shortages and high operation costs associated with EV charging can be mitigated through the use of multiple microgrids if the charging loads of EVs in the microgrids can be predicted with sufficient accuracy.

This was addressed in the present study by proposing a multi-objective multi-microgrid energy management model that considered the randomness of EV charging and adopted transmission line losses, operating costs, and carbon emissions as the targets of optimization. The charging loads of EVs were predicted using a BPNN in conjunction with LSTM deep learning correction, and an improved MOEA/D and approximate CA were adopted for solving the scheduling model.

Numerical results for a test multi-microgrid system demonstrated that the improved EV charging load prediction method reduced the prediction error by 36.86% compared with the standard BPNN method. In addition, the results of multi-objective dispatch demonstrated that the proposed MOEA/D-AMM improved the shape characteristics of the Pareto front while optimizing all objectives with a more rapid convergence than conventional MOEA/D. Furthermore the diversity of the results is also effectively improved.

Finally, research focused on deep learning has demonstrated that individual parameters such as learning efficiency can greatly affect the convergence stability of the model. In this study, a data-driven adaptive method was applied to improve convergence stability. In future research, distributed deep learning frameworks will be applied for addressing this problem. In addition, future research will implement the current multi-objective scheduling based on EV charging load data obtained in advance, rather than considering the uncertainty of EVs during the scheduling process, to improve the

Table 5
The convergence process of the objective values provided by MOEA/D.

	$f_{m,1}^{50}$	$f_{m,61}^{50}$	$f_{m,61}^{50}$	$f_{m,181}^{50}$	$f_{m,241}^{50}$	$f_{m,300}^{50}$
$m = 1$	0.01992	0.01572	0.01546	0.01532	0.01516	0.006538
$m = 2$	99,610	89,160	88,940	88,800	88,650	88,490
$m = 3$	42,780	39,090	39,030	38,970	38,900	38,760

Table 6
The convergence process of the objective values provided by MOEA/D-AMM.

	$f_{m,1}^{50}$	$f_{m,61}^{50}$	$f_{m,61}^{50}$	$f_{m,181}^{50}$	$f_{m,241}^{50}$	$f_{m,300}^{50}$
$m = 1$	0.01998	0.01644	0.01555	0.01535	0.01516	0.005892
$m = 2$	98,210	89,020	88,820	88,680	88,580	88,490
$m = 3$	42,100	39,130	39,070	38,990	38,910	38,760

Table 7

Shannon-Wiener index values obtained for the three objectives with values provided by conventional MOEA/D and proposed MOEA/D-AMM algorithms.

	SW1	SW2	SW3
MOEA/D	0.8303	0.2507	0.3798
MOEA/D-AMM	0.9085	0.2909	0.4835

real-time performance of the approach, and the robustness of microgrid scheduling will be improved by considering the uncertainty of both renewable DG and EV charging loads.

CRediT authorship contribution statement

Bifei Tan: Methodology, Software, Data curation, Writing - original draft, Visualization, Investigation, Validation, Writing - review & editing. **Haoyong Chen:** Conceptualization, Methodology, Writing - original draft, Supervision, Writing - review & editing.

Declaration of competing interest

To the best of our knowledge, the named authors have no conflict of interest.

Acknowledgments

This work was supported by the National Natural Science Foundation of China under Grant No. 51937005 and the National Key Research and Development Program of China under Grant No. 2016YFB0900100. We thank LetPub ([www.letpub.com](http://www letpub com)) for its linguistic assistance during the preparation of this manuscript.

Appendix A. Supplementary data

Supplementary data to this article can be found online at <https://doi.org/10.1016/j.energy.2020.118360>.

References

- [1] Liang Z, Chen H, Wang X, Chen S, Zhang C. Risk-based uncertainty set optimization method for energy management of hybrid AC/DC microgrids with uncertain renewable generation. *IEEE Trans Smart Grid* March 2020;11(2):1526–42. <https://doi.org/10.1109/TSG.2019.2939817>.
- [2] [a] Che L, Shahidehpour M, Alabdulwahab A, Al-Turki Y. Hierarchical coordination of a community microgrid with AC and DC microgrids. *IEEE Trans Smart Grid* Nov. 2015;6(6):3042–51. <https://doi.org/10.1109/TSG.2015.2398853.C>. [b] Moreira L, Resende FO, Lopes JAP. Using low voltage MicroGrids for service restoration. *IEEE Trans Power Syst* Feb. 2007;22(1):395–403. <https://doi.org/10.1109/TPWRS.2006.888989>.
- [3] Karimi Hamid, Javid Shahram. Optimal microgrid operation scheduling by a novel hybrid multi-objective and multi-attribute decision-making framework. *Energy* 2019;186. <https://doi.org/10.1016/j.energy.2019.115912>, 115912, ISSN 0360-5442.
- [4] Pourghasem Pouya, Sohrabi Farnaz, Abapour Mehdi, Mohammadi-Ivatloo Behnam. Stochastic multi-objective dynamic dispatch of renewable and CHP-based islanded microgrids. *Elec Power Syst Res* 2019;173:193–201. <https://doi.org/10.1016/j.epsr.2019.04.021>.
- [5] Ahmadi A, Swanson AG, Van Coller J. NonConvex optimisation of combined environmental economic dispatch through cultural algorithm with the consideration of the physical constraints of generating units and price penalty factors. *SAIEE Africa Res J Sept.* 2016;107(3):146–66.
- [6] Dey Bishwajit, Roy Shyamal Krishna, Bhattacharyya Biplab. Solving multi-objective economic emission dispatch of a renewable integrated microgrid using latest bio-inspired algorithms. *Eng Sci Technol, Int J* 2019;22(1). [https://doi.org/10.1016/j.jestch.2018.10.001](https://doi.org/10.1016/jjestch.2018.10.001). 55–66, ISSN 2215-0986.
- [7] Ma Haiping, Yang Zhile, You Pengcheng, Fei Minrui. Multi-objective biogeography-based optimization for dynamic economic emission load dispatch considering plug-in electric vehicles charging. *Energy* 2017;135. <https://doi.org/10.1016/j.energy.2017.06.102>. 101–111, ISSN 0360-5442.
- [8] Chandrasekaran K, Simon SP, Padhy NP. Cuckoo search algorithm for emission reliable economic multi-objective dispatch problem. *IETE JRes* 2014;60:128–38. <https://doi.org/10.1080/03772063.2014.901592>.
- [9] Li Y, Wang P, Gooi HB, Ye J, Wu L. Multi-objective optimal dispatch of microgrid under uncertainties via interval optimization. *IEEE Trans Smart Grid* March 2019;10(2):2046–58. <https://doi.org/10.1109/TSG.2017.2787790>.
- [10] Coelho Vitor N, Coelho Igor M, Coelho Bruno N, Weiss Cohen Miri, Reis Agnaldo JR, Silva Sidelmo M, Marcone J, Souza F, Fleming Peter J, Guimaraes Frederico G. Multi-objective energy storage power dispatching using plug-in vehicles in a smart-microgrid. *Renew Energy* 2016;89. <https://doi.org/10.1016/j.renene.2015.11.084>. 730–742, ISSN 0960-1481.
- [11] Xu Zhirong, Yang Ping, Zheng Chengli, Zhang Yujia, Peng Jiajun, Zeng Zhiji. Analysis on the organization and Development of multi-microgrids. *Renew Sustain Energy Rev* 2018;81(2):2204–16. <https://doi.org/10.1016/j.rser.2017.06.032>.
- [12] [a] Esmaili M, Shafiee H, Aghaei J. Range anxiety of electric vehicles in energy management of microgrids with controllable loads. *J Energy Stor* 2018;20:57–66. [b] Hou H, Xue M, Xu Y, Xiao Z, Deng X, Xu T, et al. Multi-objective economic dispatch of a microgrid considering electric vehicle and transferable load. *Appl Energy* 2020;262:114489. <https://doi.org/10.1016/j.apenergy.2020.114489>.
- [13] Haidar AMA, Muttaqi KM. Behavioral characterization of electric vehicle charging loads in a distribution power grid through modeling of battery chargers. *IEEE Trans Ind Appl* Jan.-Feb. 2016;52(1):483–92. <https://doi.org/10.1109/TIA.2015.2483705>.
- [14] Carlos Gómez J, Morcos MM. Impact of EV battery chargers on the power quality of distribution systems. *IEEE Trans Power Deliv* Jul. 2003;18(3):975–81. <https://doi.org/10.1109/tpwr.2002.4311766>.
- [15] Huang X, Xu C, Wang P, Liu H. LNSC: a security model for electric vehicle and charging pile management based on blockchain ecosystem. *IEEE Access* 2018;6:13565–74. <https://doi.org/10.1109/ACCESS.2018.2812176>.
- [16] Chen Qifang, Wang Fei, Hodge Bri-Mathias, Zhang Jianhua, Li Zhigang, Shafeikhan, Miadreza, Catalao Joao. Dynamic price vector formation model-based automatic demand response strategy for PV-assisted EV charging stations. *IEEE transactions on smart grid*. 2017. <https://doi.org/10.1109/TSG.2017.2693121>. 1–1.
- [17] Kim Y, Kwak J, Chong S. Dynamic pricing, scheduling, and energy management for profit maximization in PHEV charging stations. *IEEE Trans Veh Technol* Feb. 2017;66(2):1011–26. <https://doi.org/10.1109/TVT.2016.2567066>.
- [18] Lu Xinhui, Zhou Kaile, Yang Shanlin. Multi-objective optimal dispatch of microgrid containing electric vehicles. *J Clean Prod* 2017;165:1572–81. <https://doi.org/10.1016/j.jclepro.2017.07.221>. ISSN 0959-6526.
- [19] Han S, Han S, Sezaki K. Optimal control of the plug-in electric vehicles for V2G frequency regulation using quadratic programming. In: Innovative SmartGrid technologies; 2011. p. 1–6. <https://doi.org/10.1109/ISGT.2011.5759172>.
- [20] Esmaili M, Shafiee H, Aghaei J. Range anxiety of electric vehicles in energy management of microgrids with controllable loads. *J Energy Stor* 2018;20:57–66. <https://doi.org/10.1016/j.est.2018.08.023>.
- [21] Iacobucci R, McLellan B, Tezuka T. Costs and carbon emissions of shared autonomous electric vehicles in a Virtual Power Plant and Microgrid with renewable energy. *Energy Procedia* 2019;156:401–5. <https://doi.org/10.1016/j.egypro.2018.11.104>.
- [22] Jiang H, Ning S, Ge Q. Multi-objective optimal dispatching of microgrid with large-scale electric vehicles. *IEEE Access* 2019;7:145880–8. <https://doi.org/10.1109/ACCESS.2019.2945597>.
- [23] Li Bei, Roche Robin. Optimal scheduling of multiple multi-energy supply microgrids considering future prediction impacts based on model predictive control. *Energy* 2020;197:117180. <https://doi.org/10.1016/j.energy.2020.117180>. ISSN 0360-5442.
- [24] Shi Ruifeng, Li Shaopeng, Zhang Penghui, Lee Kwang Y. Integration of renewable energy sources and electric vehicles in V2G network with adjustable robust optimization. *Renew Energy* 2020;153:1067–80. <https://doi.org/10.1016/j.renene.2020.02.027>. ISSN 0960-1481.
- [25] Ying Hao, Dong Lei, Liang Jun, Liao Xiaozhong, Wang Lijie, Shi Lefeng. Power forecasting-based coordination dispatch of PV power generation and electric vehicles charging in microgrid. *Renew Energy* 2020;155:1191–210. <https://doi.org/10.1016/j.renene.2020.03.169>. ISSN 0960-1481.
- [26] Lu Xinhui, Zhou Kaile, Yang Shanlin, Liu Huizhou. Multi-objective optimal load dispatch of microgrid with stochastic access of electric vehicles. *J Clean Prod* 2018;195:187–99. <https://doi.org/10.1016/j.jclepro.2018.05.190>.
- [27] Jahangir Hamidreza, Tayarani Hanif, Ali Ahmadian, Golkar Masoud Aliakbar, Miret Jaume, Tayarani Mohammad, Oliver Gao H. Charging demand of plug-in electric vehicles: forecasting travel behavior based on a novel rough artificial neural network approach. *J Clean Prod* 2019;229:1029–44. <https://doi.org/10.1016/j.jclepro.2019.04.345>.
- [28] Karasú Seçkin, Altan Aytaç, Sarac Zehra, Hacioglu Rifat. Estimation of fast varied wind speed based on Narx neural network by using curve fitting. 2017.
- [29] Baghaee Hamid Reza, Mirsalim Mojtaba, Gharehpetian GB, Talebi HA. Application of RBF neural networks and unscented transformation in probabilistic power-flow of microgrids including correlated wind/PV units and plug-in hybrid electric vehicles. *Simulat Model Pract Theor* 2017;72:51–68. <https://doi.org/10.1016/j.simpat.2016.12.006>.
- [30] Nassih Bouchra, Amine Aouatif, Ngadi Mohammed, Hmina Nabil. DCT and HOG feature sets combined with BPNN for efficient face classification. *Procedia Comput Sci* 2019;148:116–25. <https://doi.org/10.1016/j.procs.2019.01.015>. ISSN 1877-0509.
- [31] Li B. Innovative target tracking method combined adaptive \$\alpha\$-\$\beta\$ filter with robust BPNN. *IEEE Access* 2019;7:60299–309. <https://doi.org/10.1109/ACCESS.2019.2733310>.

- [10.1109/ACCESS.2019.2915381](https://doi.org/10.1109/ACCESS.2019.2915381).
- [32] Makarenkov Victor, Rokach Lior, Shapira Bracha. Choosing the right word: using bidirectional LSTM tagger for writing support systems. *Eng Appl Artif Intell* 2019;84:1–10. <https://doi.org/10.13140/RG.2.2.12567.01446>.
- [33] Altan Aytac, Karasu Seckin, Bekiros Stelios. Digital currency forecasting with chaotic meta-heuristic bio-inspired signal processing techniques. *Chaos. Solitons & Fractals* 2019;126:325–36. ISSN 0960-0779, <https://doi.org/43.webvpn.scut.edu.cn/10.1016/j.chaos.2019.07.011>.
- [34] Ergen T, Kozat SS. Online training of LSTM networks in distributed systems for variable length data sequences. *IEEE Transactions on Neural Networks and Learning Systems* Oct. 2018;29(10):5159–65. <https://doi.org/10.1109/TNNLS.2017.2770179>.
- [35] Chen S, Song B, Guo J. Attention alignment multimodal LSTM for fine-gained common space learning. *IEEE access*, vol. 6; 2018. p. 20195–208. <https://doi.org/10.1109/ACCESS.2018.2822663>.
- [36] Yang Y, et al. Video captioning by adversarial LSTM. *IEEE Trans Image Process* Nov. 2018;27(11):5600–11. <https://doi.org/10.1109/TIP.2018.2855422>.
- [37] Tang X. Large-scale computing systems workload prediction using parallel improved LSTM neural network. *IEEE Access* 2019;7:40525–33. <https://doi.org/10.1109/ACCESS.2019.2905634>.
- [38] Yang P, Tang K, Yao X. Turning high-dimensional optimization into computationally expensive optimization. *IEEE Trans Evol Comput* Feb. 2018;22(1):143–56. <https://doi.org/10.1109/TEVC.2017.2672689>.
- [39] Subramanian R, Thanushkodi K, Neelakantan PN. Solution of economic load dispatch problems with valve-point effect using Novel TANAN's Algorithm. In: 2013 international conference on current trends in engineering and technology (ICCTET), coimbatore; 2013. p. 141–5. <https://doi.org/10.1109/ICCTET.2013.6675930>.
- [40] Zhang Z, Zhang Y, Huang Q, Lee W. Market-oriented optimal dispatching strategy for a wind farm with a multiple stage hybrid energy storage system. *CSEE J Power Energy Syst* Dec. 2018;4(4):417–24. <https://doi.org/10.17775/CSEEPES.2018.00130>.
- [41] Ta-Yuan Hsu Ajay D Kshemkalyani, Shen Min. Causal consistency algorithms for partially replicated and fully replicated systems. *Future Generat Comput Syst* 2018;86:1118–33. <https://doi.org/10.1016/j.future.2017.04.044>.
- [42] Chen S, Ho DWC, Li L, Liu M. Fault-tolerant consensus of multi-agent system with distributed adaptive protocol. *IEEE Trans Cybern* Oct. 2015;45(10):2142–55. <https://doi.org/10.1109/TCYB.2014.2366204>.
- [43] Yin Peng-Yeng, Wu Tsai-Hung, Hsu Ping-Yi. Simulation based risk management for multi-objective optimal wind turbine placement using MOEA/D. *Energy* 2017;141:579–97. <https://doi.org/10.1016/j.energy.2017.09.103>.
- [44] Karbalaei Farid, Shahbazi Hamidreza. Determining an appropriate partitioning method to reduce the power system dimensions for real time voltage control. *Int J Electr Power Energy Syst* 2018;100:58–68. <https://doi.org/10.1016/j.ijepes.2018.02.025.19>.
- [45] Douthe Cyril, Romain mesnil, hugo orts, olivier baverel, isoradial meshes: covering elastic gridshells with planar facets. *Autom ConStruct* 2017;83. <https://doi.org/10.1016/j.autcon.2017.08.015>. 222–236, ISSN 0926-5805.
- [46] Strong WL. Biased richness and evenness relationships within Shannon–Wiener index values. *Ecol Indicat* 2016;67. <https://doi.org/10.1016/j.ecolind.2016.03.043>. 703–713, ISSN 1470-160X.



BIFEI TAN received the B.E. degree in electrical engineering and automation from South China University of Technology, China, in 2013 and 2017. He is currently pursuing the Ph.D. degree with the power system and its automation, South China University of Technology, China. His current research interests include economic dispatch in micro-grid, machine learning, energy transfer systems, and wind power forecasting.



HAOYONG CHEN (M'03–SM'10) received the B.S., M.S., and Ph.D. degrees in electrical engineering from Xian Jiaotong University, Xi'an, China, in 1995, 1997, and 2000, respectively. He is currently a Professor with the School of Electric Power, South China University of Technology, Guangzhou, China. He is also the Chair of Asia–Pacific Research Institute of Smart Grid and Renewable Energy, Hong Kong. His current research interests include power system operation/control, smart grids, computational intelligence applications and power markets.